Two-dimensional effects on electrostatic instabilities in Hall thrusters. I. Insights from particle-in-cell simulations and two-point power spectral density reconstruction techniques

Federico Petronio, Thomas Charoy, Alejandro Alvarez Laguna, Anne Bourdon, Pascal Chabert

Two-dimensional effects on electrostatic instabilities in Hall Thrusters. I. Insights from particle-in-cell simulations and two-point power spectral density reconstruction techniques.

Federico Petronio,[1,2] Thomas Charoy,[1] Alejandro Alvarez Laguna,[1] Anne Bourdon,[1] and Pascal Chabert[1]

[1)]*Laboratoire de Physique des Plasmas (LPP), CNRS, Sorbonne Université, École Polytechnique, Institut Polytechnique de Paris, 91120 Palaiseau, France.*

[2)]*Safran Aircraft Engines, Electric Propulsion Unit, 27208 Vernon, France.*

(*Electronic mail: federico.petronio@lpp.polytechnique.fr)

(Dated: 13 October 2022)

Using 2D Particle-in-Cell (PIC) simulations coupled to a fluid description of the gas dynamics, we study the electrostatic instabilities developing in the axial-azimuthal plane of a Hall Thruster, during several periods of a low-frequency oscillation (the so-called breathing mode at 10 kHz). As done in experiments, the 2D PIC-MCC code is coupled to an electrical circuit in order to partially damp the (otherwise large) discharge current fluctuations at the breathing mode frequency. The different electrostatic higher frequency modes that develop in the plasma are analyzed using a two-point power spectral density reconstruction method, which allows to generate the dispersion diagrams (in the frequency-wavenumber space) along the axial and azimuthal directions, and at different times during the low-frequency breathing mode oscillations. This technique allows to distinguish between different well-identified instabilities: the electron cyclotron drift instability (ECDI) and its evolution towards an ion acoustic wave (IAW) and the ion transit-time instability (ITTI). These instabilities are usually considered unidirectional (either axial or azimuthal), however, it is shown here that they exist in both directions. This two-dimensional character is instrumental in understanding where these instabilities grow and how they propagate in the thruster channel and plume. A theoretical discussion of this aspect is proposed in a companion paper (part II). The effects of (i) the azimuthal length of the simulation box, and (ii) the electron temperature injection at the cathode, are also discussed.

I. INTRODUCTION

Hall thrusters (HTs) have been successfully used in space missions for more than 60 years[1–3]. The plasma discharge chamber has an annular shape, and the walls are usually made of dielectric materials. A neutral gas, usually xenon, is injected through the anode into the chamber where it is ionized and the resulting charged ions are accelerated towards the open end. The discharge is sustained thanks to electrons emitted by a hollow cathode, external to the channel, which also emits the electrons required to neutralize the positively charged ion beam exiting the thruster. The voltage difference between the cathode and the anode (typically $\sim 300\,\mathrm{V}$) generates an electric field along the chamber axis that accelerates the ions downstream to generate the thrust. A stationary magnetic field, directed radially, generates an $\mathbf{E}\times\mathbf{B}$ configuration. As a consequence, electrons have a large drift in the $\mathbf{E}\times\mathbf{B}$ (azimuthal) direction, with a velocity much higher than the cross-field drift velocity along the channel. The current in the $\mathbf{E}\times\mathbf{B}$ direction increases the residence time of electrons inside the discharge chamber, enhancing ionization of the injected neutral gas. The ion Larmor radius is larger than the device dimensions and ions can be considered as not magnetized.

Plasma discharges with an $\mathbf{E}\times\mathbf{B}$ cross-field configuration are used in several low-temperature plasma devices, such as magnetron sputtering systems[4]. The physics of these discharges has been the subject of active research from theoretical[1,5–9], numerical[10–12] and experimental[13,14] points of view. It has been shown[12,15,16] that plasma instabilities play a fundamental role in $\mathbf{E}\times\mathbf{B}$ discharges, and that they, along with their coupling with turbulence[9], could be responsible for the anomalous electron mobility observed in the axial direction. Several instabilities have been identified and studied in HTs. These instabilities cover a large range of frequencies, including: (1) the so-called Breathing Mode (BM)[17–20] at $\approx 10\,\mathrm{kHz}$, (2) the Ion Transit-Time Instability (ITTI)[21–24] at $\approx 500\,\mathrm{kHz}$, (3) the Modified Two-Streams Instability (MTSI)[25–28] at $\approx 1\,\mathrm{MHz}$, (4) the Electron Cyclotron Drift Instability (ECDI)[6,8,15,25,29–33] and (5) the evolution of the ECDI towards an Ion Acoustic Wave (IAW)[16,27,34], at $\approx 8\,\mathrm{MHz}$. However, the origin, the growth and the saturation mechanisms of some of the above instabilities remain unclear (see for instance the different theories proposed for the BM[18,19], or the partial theoretical treatment of the IAW[16] or the ITTI[21]).

In recent years, the easier access to high-performance computing resources has resulted in an increasing interest in using PIC codes to study HTs; 2D PIC radial-azimuthal and axial-azimuthal simulations have been used to study electrostatic instabilities in $\mathbf{E}\times\mathbf{B}$ discharges[12,28,35,36]. In

order to study the coupling between the BM, ITTI, and IAW, Charoy *et al.*[24] coupled a PIC simulation of the plasma dynamics in the axial-azimuthal plane of the HT with a configuration similar to the one proposed by Boeuf and Garrigues[37] to a 1D fluid code that models the neutral dynamics. The work by Charoy *et al.* treats self-consistently the collisions between the gas and the plasma species (ions and electrons) including elastic, backscattering, excitation, and ionization collisions. As a result, the simulations are able to capture the low-frequency BM oscillations. However, these 2D PIC simulations are computationally very expensive and require tens of days on thousands of CPUs. For these reasons, the authors used a permittivity scaling technique[30,38] and a reduced azimuthal length (few centimeters). Charoy *et al.*[24] observed that the simulation results are strongly influenced by the azimuthal domain lengths. Above $L_y = 2\,\mathrm{cm}$, it was found that the discharge current oscillations were much stronger than those observed in experiments, which in most cases are damped by external electrical circuits. These large current oscillations dramatically increase the computational cost as the plasma density becomes very large when the current is maximal, and the discharge may extinguish when the current collapses.

In this paper, the effect of the scaled permittivity and of the azimuthal length on the PIC simulation results are discussed. In addition, an external circuit has been coupled to the PIC-neutral gas simulations, as previously done by Barral *et al.*[39] with a 1D fluid model. As mentioned above, HT devices use such electrical circuits to filter out the oscillations. The discretization scheme of the circuit equations coupled to the PIC code is described in details. This provides a unique simulation tool that couples PIC simulations of charged particles, fluid equations for the neutral gas dynamics, and circuit equations to treat the system electrodynamics. As it will be shown, this configuration partially damps the simulated BM oscillations, as observed in real experiments.

This work also addresses the issue of spectral analysis of the fluctuations in 2D and in situations in which spatial gradients may be significant. In previous works, the instability spectrum in the periodic azimuthal direction has been obtained using the standard Discrete Fourier Transform (DFT) techniques[25,27,28,32]. However, when the plasma dynamics is coupled to that of the neutral gas, modes that have mainly an axial component (BM and ITTI) appear. The strong plasma inhomogeneities in the axial direction disqualify the DFT technique in such a situation. In order to overcome this difficulty, the two-point power spectral density (PSD2P) approach has been used here. The technique has been developed by Beall *et al.*[40] and Dudok de Wit *et al.*[41], and previously used in the study of HTs by Fernandez *et al.*[21] in radial-axial simulations and, more recently, in the analysis of experimental data by Brown & Jorns[42], to study the macroscopic features of the

spectrum in the plasma plume. The idea is to reconstruct the spectrum by using the signal from a set of point pairs, that can be close in space. It allows to calculate the power spectral density (PSD) along the axial direction, at a chosen axial position, with an excellent resolution, and therefore to reveal the spectrum spatial evolution. The benefit of this technique to characterize the direction of the propagation of the electrostatic instabilities during the BM with increased accuracy as compared to standard DFTs will be demonstrated. The current work completes and extends the studies of previous works[24,34], where the spectral analysis in the axial direction was not carried out.

The structure of this paper is as follows. The simulation model is described in Section II, and the details of the circuit design and its implementation is treated in Section III. The PSD2P technique is discussed in Section IV and is subsequently applied to PIC data. It is shown that this technique allows to capture the electron cyclotron drift instability (ECDI), the ion acoustic wave (IAW) and the ion transit-time instability (ITTI). These instabilities are usually considered monodimensional, but it is observed here that their signature can be observed in the spectrum of both directions. This essential observation is used in Paper II to propose some hypothesis about the origin of the electrostatic instabilities in HTs. This companion paper relies on a general derivation of a 3D fluid dispersion relation (DR) for electrostatic instabilities, from which analytical DRs of the various modes (IAW, MTSI and ITTI) can be obtained in 2D and directly compared to the PSD2P dispersion plots.

II. DESCRIPTION OF THE PIC SIMULATION SETUP

The simulations are obtained with *LPPic*[35], a 2D3V Particle-in-Cell Monte Carlo Collision (PIC-MCC) code, that is used to simulate $\mathbf{E}\times\mathbf{B}$ discharges. The MCC module and the PIC modules in a quasi-1D configuration have been validated against the benchmark proposed by Turner *et al.*[43] and the 2D PIC has reproduced recent benchmarks on $\mathbf{E}\times\mathbf{B}$ discharges in axial-azimuthal (xy) and in radial-azimuthal (zy) planes[28,36]. The simulation setup that is used in the present work is the one that is described extensively by Charoy *et al.*[24,36]. We refer the reader to these works for more details and, hereafter, we will mention the main code characteristics.

LPPic is written in Fortran and parallelized with MPI. As sketched in Figure 1, the domain consists in a structured Cartesian mesh with axial and azimuthal lengths, L_x and L_y, respectively. The axial length $L_x = 4\,\text{cm}$ includes the discharge channel (between the anode at $x = 0$ and $x = 2.5\,\text{cm}$) and part of the plume for $2.5 \leq x \leq 4\,\text{cm}$. The curvature of the channel is not considered and pe-

riodic boundaries are imposed in the azimuthal direction. The Poisson equation is solved in the 2D xy-plane and radial (along z) effects are not taken into account. The voltage at the cathode (right boundary) is fixed to zero, while the anode (left boundary) voltage is controlled by an electric circuit, which is described in the next section, with a DC voltage generator set to 300 V. The magnetic field is in the z-direction, and it varies along the thruster axis as shown by the purple line in Figure 1, while it is constant along the azimuthal direction. Its maximal value is set to 170 G at the exit plane of the thruster channel.

A 1D fluid model is used for the neutral gas dynamics which is self-consistently coupled to the charged species dynamics through collisions, as explained in Charoy *et al.*[24]. The plasma is initialized with an homogeneous density and at later times the discharge is sustained by ionization (within the MCC module). The neutral gas is also initialized with a constant density and a constant mass flow of $\dot{m} = 5\,\mathrm{mg\,s^{-1}}$ of neutral gas is injected at the anode. In addition to the imposed neutral flux, the anode boundary condition also accounts for neutrals produced from ion recombination at the anode. At the other boundary, the cathode, Neumann conditions are imposed in order to simulate an open boundary for the neutral gas fluid. The neutral dynamics is modeled with the Euler isothermal equations. The equations are discretized with a cell-centered finite volume scheme that uses an HLLC Riemann solver[44] with a relaxation scheme that ensures the temperature to be at 640 K. More details about the coupling between the fluid and the PIC codes and the numerical implementation can be found in Charoy *et al.*[24].

Electrons are injected at the grounded cathode. It will be shown that the cathode model and the electron injection temperature have an influence on the discharge and the steady-state characteristics. For the injection, we consider a quasi-neutrality assumption, which assumes that at each time step we emit uniformly a number of electrons that compensate the charge at the cathode boundary. For a detailed description of the electron injection the reader should refer to Ref[24].

The plasma density strongly varies during a BM oscillation and consequently the time step Δt and the cell size Δx are constrained by the peak densities. According to Birdsall and Langdon[45], the stability constraints of an explicit PIC simulation requires $\Delta t \leq 0.2/\omega_{pe}$, where $\omega_{pe} = \sqrt{m_e \varepsilon_0 / n_e e^2}$ is the electron plasma frequency and $\Delta x \leq \lambda_D$ where $\lambda_D = \sqrt{\varepsilon_0 k_b T_e / n_e e^2}$ is the electron Debye length. In the above expressions, ε_0 stands for the vacuum permittivity, m_e is the electron mass, e is the electron charge, k_b is the Boltzmann constant and T_e is the electron temperature. Given the typical parameters of the discharge studied here, the time step and cell size are fixed to 2×10^{-12} s and 2×10^{-5} m. All the simulation parameters are summarized in Table I.

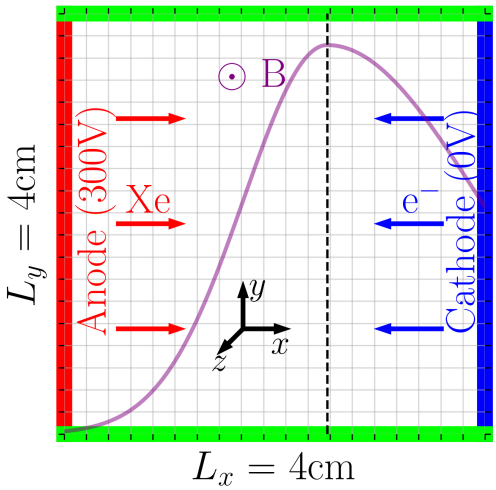

FIG. 1: The simulation mesh is composed by squared cells. The neutral gas is injected at the anode (left) and the electrons at the cathode (right). The axis of the thruster is x and the azimuthal direction is y. We use periodic boundary conditions in the azimuthal direction. The magnetic field intensity is represented by the purple line. It is perpendicular to the simulation plane (along z) and does not change along the azimuthal direction. Please refer to Table I for a detailed list of the simulation parameters.

A simulation with these numerical parameters is extremely costly in order to capture several BM periods. To relax the PIC constraints a permittivity scaling technique, as already done in Refs[24,30,38], has been used. Using an effective (increased) permittivity $\varepsilon_0^* = \alpha^0 \varepsilon_0$ we can increase the time step and cell size and hence reduce the simulation time. In the present work, $\alpha^0 = 64$ has been used, leading to an increase of both Δt and Δx by a factor of 8.

A. Impact of the scaled permittivity on the instabilities

The permittivity scaling technique is known to have an impact on the discharge physics[30]. In particular, Charoy *et al.*[24,34] noticed that an increased permittivity affects some of the instabilities characteristics. A detailed discussion of the electrostatic instabilities properties is provided in the

the companion paper (Part II). In the present section we limit our analysis to the macroscopic effects of the scaled permittivity on the ECDI, IAW and ITTI, which are the dominant axial-azimuthal electrostatic instabilities. The scaled permittivity could also have some consequences on the frequency and amplitude of the BM. In this work this aspect is not addressed.

Cavalier *et al.*[6] numerically solved the kinetic DR of the ECDI. Their results show that the ECDI DR depends on the ratio ω_{ce}/ω_{pi}, where $\omega_{ce} = eB/m_e$ is the electron cyclotron frequency and $\omega_{pi} = \sqrt{n_i e^2/(m_i \varepsilon_0)}$ is the ion plasma frequency. The ECDI resonances appear at fixed values of k_y, which do not depend on the vacuum permittivity. However, the frequency of the wave at maximum growth rate and, even more important, the growth rate itself largely depend on the permittivity. Charoy *et al.* observed longer wavelengths[24,36] when introducing a permittivity scaling.

It has been observed in PIC simulations that the ECDI evolves in reasonably short time scales towards an Ion Acoustic Wave (IAW) as its amplitude grows[16,24,27,42,46]. Lafleur *et al.*[8] have shown that the wavenumber and frequency, corresponding to the maximum growth rate read

$$k_y^{\max} = \frac{1}{\sqrt{2}\lambda_D} \propto \frac{1}{\sqrt{\alpha^0}} \quad \text{and} \quad \omega^{\max} \simeq \frac{\omega_{pi}}{\sqrt{3}} \propto \frac{1}{\sqrt{\alpha^0}},$$

respectively. Considering the results of the aforementioned works, we expect for our scaled case that the frequency of the IAW is in the $(500\,\mathrm{kHz} - 1\,\mathrm{MHz})$ range and its wavenumber in the $(150\,\mathrm{m}^{-1} - 1000\,\mathrm{m}^{-1})$ range. Since the IAW instability can be seen as the limit of the ECDI, in the current work we will refer in some circumstances to the ECDI/IAW instability. The link between the kinetic ECDI and the fluid IAW will be further discussed in Paper II.

Fernandez *et al.*[21] have shown that the ITTI DR relation does not depend on the permittivity scaling and this has been confirmed by Charoy *et al.*[24], who reported that the ITTI frequency was nearly independent of the scaling factor. The major impact of the scaling is on the oscillations amplitude. This is consistent with the observation of Fernandez, who suggested that the ITTI growth rate is proportional to the electron mobility (i.e. $\gamma_{ITTI} \propto \mu_e^{-1/2}$), that is reduced when the scaling factor increases (most likely because the anaomalous mobility is governed by the ECDI, which as noted above is affected by the permittivity scaling). Therefore, the ITTI is expected to be at a frequency of $\approx 500\,\mathrm{kHz}$ in the $(20\,\mathrm{m}^{-1} - 200\,\mathrm{m}^{-1})$ wavenumber range.

One should however be aware that the coupling between the modes, in particular between the ITTI and the ECDI is most likely non-linear, which makes difficult to fully predict the exact impact of the permittivity scaling on the instabilities dynamics.

B. Impact of the azimuthal domain length on the instabilities

The choice of the azimuthal length of the domain is a compromise between the computational cost and the resolution of the azimuthal wavenumber spectrum. In particular, as discussed above, the wavelength of some azimuthal instabilities are increased by the permittivity scaling. In order to successfully apply the PSD reconstruction technique (described in Section IV), a rather large number of azimuthal points is required. For these reasons, we used an azimuthal length of $L_y = 4\,\text{cm}$, that is larger than the ones usually used in previous works[30,36,37].

The choice of the azimuthal length also impacts the dynamics of the breathing mode. Charoy *et al.*[24,34] studied similar conditions to the ones studied in this paper and showed that for azimuthal lengths larger than 4 cm, the discharge current oscillations over a BM period can become very strong and drive the plasma into some unrealistic conditions (at least conditions not seen in experiments). For this reason, as done in real devices, an external electrical circuit has been used to drive the discharge. With this circuit, the voltage across the discharge varies in time, and the discharge current oscillations are partially damped. This allows to simulate larger azimuthal domains with more realistic discharge current oscillations. The circuit model is presented in the next section.

III. RLC CIRCUIT MODEL

HT devices are powered by a DC generator and are equipped of an *RLC* filter that controls the anode voltage[39]. The filter, sketched in Figure 2, is composed of a resistor R and inductance L set in parallel, and a capacitance C in series.

A. Circuit equations and coupling with the PIC code

Using Kirchhoff's circuit laws, we obtain:

$$\begin{cases} I = I_r + I_l - I_c, \\ U = U_r - U_g, \\ I_c = C\dfrac{dU}{dt}, \\ U_l = U_r = RI_r = L\dfrac{dI_l}{dt}. \end{cases} \tag{1}$$

Where U_g is the DC applied voltage and the voltage drop at the plasma boundaries and the discharge current are U and I, respectively. The indices r, l and c are used to define the voltage

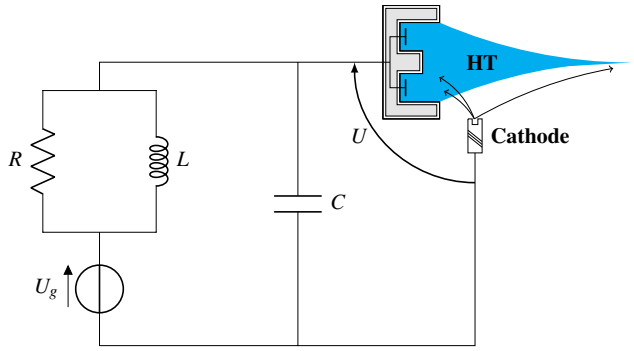

FIG. 2: Scheme of the circuit of an HT. The generator applies a DC voltage U_g. The voltage drop at the plasma boundaries and the discharge current are U and I, respectively.

drop and current flowing in the different circuit components and d/dt represents the temporal derivative. With some algebraic manipulation the above system simplifies to

$$\begin{cases} \dfrac{dI_r}{dt} + \dfrac{R}{L}\dfrac{dI_r}{dt} = C\dfrac{d^2U}{dt^2} + \dfrac{dI}{dt}, \\ I_r = \dfrac{U_g - U}{R}. \end{cases} \tag{2}$$

Let $\Delta U = U - U_g$, then the evolution of the circuit may be written as an ordinary differential equation for this variable, as follows,

$$C\frac{d^2\Delta U}{dt^2} + \frac{1}{R}\frac{d\Delta U}{dt} + \frac{1}{L}\Delta U = -\frac{dI}{dt}. \tag{3}$$

The equation above can be discretized and solved numerically, using the following temporal discretization,

$$\begin{cases} \dfrac{d^2\Delta U}{dt^2} = \dfrac{\Delta U_n - 2\Delta U_{n-1} + \Delta U_{n-2}}{\Delta t_{RLC}^2} + O\left(\Delta t_{RLC}^2\right), \\ \dfrac{d\Delta U}{dt} = \dfrac{\Delta U_n - \Delta U_{n-1}}{\Delta t_{RLC}} + \dfrac{\Delta t_{RLC}}{2}\dfrac{d^2\Delta U}{dt^2} + O\left(\Delta t_{RLC}^2\right) = \dfrac{3\Delta U_n - 4\Delta U_{n-1} + \Delta U_{n-2}}{2\Delta t_{RLC}} + O\left(\Delta t_{RLC}^2\right), \\ \dfrac{dI}{dt} = \dfrac{I_{n-1} - I_{n-2}}{\Delta t_{RLC}} + O\left(\Delta t_{RLC}\right). \end{cases}$$

The circuit equation is solved every N_{RLC} PIC loops in order to average the current and avoid high-frequency noise. So, in the above equation, the *RLC* timestep can be defined as a function of the PIC timestep Δt, as $\Delta t_{RLC} = N_{RLC} \cdot \Delta t$. The discretization scheme is a second order scheme for the voltage, while it is first order for the current (calculated in PIC simulations), which means that overall the scheme is first order.

The voltage at the anode is set to $U_n = U(t = n \cdot \Delta t_{RLC})$, that is computed as $U_n = U_g + \Delta U_n$ from the following equation

$$\Delta U_n = \frac{L}{2RLC + 3L\Delta t_{RLC} + 2R\Delta t_{RLC}^2} \left(4(RC + \Delta t_{RLC})\Delta U_{n-1} - (2RC + \Delta t_{RLC})\,\Delta U_{n-2} - 2R\Delta t_{RLC}\,(I_{n-1} - I_{n-2})\right). \tag{4}$$

The current is averaged over N_{RLC} loops and Eq. (4) is solved using the current and voltage values at the previous time-steps to find the new anode voltage. This voltage is kept constant for the subsequent N_{RLC} time-steps. The results presented here are obtained using $N_{RLC} = 250$, which allows to resolve the breathing mode with ~ 7500 timesteps.

B. Plasma Transfer Function and choice of circuit parameters

Two sets of circuit element values have been tested. The first set uses values implemented in some real HT devices and close to those used in Ref.[39]: $R = 60\,\Omega$, $L = 340\,\mu$H and $C = 10\,\mu$F. This set is labeled "standard" in the following. The second set is found by analyzing the circuit transfer function. The linear frequency response of the circuit between the discharge electrodes in Laplace formalism reads

$$\mathbf{G}(s) = \frac{RLCs^2 + Ls + R}{RLs}. \tag{5}$$

This equation is used to choose R, L and C values to limit the discharge current oscillations in the conditions studied in this work. In Figure 3, we plot the Bode diagram of Eq. 5 for $R = 60\,\Omega$, $L = 4.4\,$mH and $C = 15\,$nF. This set is labeled "optimized" in the following. As shown in Figure 3, with these values, the filter is adapted to damp the oscillations with a frequency around ~ 20kHz, i.e. near the BM frequency. However, as the discharge response is non-linear, we can expect that the circuit will not be able to completely filter out the current oscillations in the PIC simulations.

IV. THE TWO POINTS PSD RECONSTRUCTION TECHNIQUE

The study of the spectrum along the axial direction (x-direction in Fig. 1) of a HT is problematic since the plasma presents strong gradients in this direction. In a standard fast Fourier transform (FFT), the wavenumber spectral resolution is determined by the number of grid points of the simulation. As a result, in order to have enough resolution in the computation of the axial wavenumber spectrum, one has to consider points with different plasma conditions as the x-direction is not

TABLE I: Operating and numerical parameters used in PIC simulations. With a small axial-azimuthal domain (4 cm × 1 cm), 3 simulation cases are considered: one without circuit and cases 1 and 2 with circuits. With a larger axial-azimuthal simulation domain (4 cm × 4 cm), 3 simulation cases are considered: one without circuit and cases A and B with circuits.

Physical parameters	Symbol	Value	Unit
Gas		Xenon	(-)
Radial magnetic field (max)	B	170	G
Anode voltage	V_a	300	V
Cathode voltage	V_c	0	V
Axial length	L_x	4	cm
Azimuthal length	L_y	1.01 or 4.08	cm
Initial plasma density	n_0	5×10^{18}	m^{-3}
Initial electron temperature	T_e	1	eV
Initial ion temperature	T_i	0.05	eV
Neutral mass flow rate	$\dot{m}$	5	$mg\,s^{-1}$
Thruster section	$Area$	3.768×10^{-3}	m^2
Cathode injection temperature (all cases except case B)	T_e^{cath}	5	eV
Cathode injection temperature (case B)	T_e^{cath}	0.1	eV
Circuit parameters (for Case 1 / Cases 2 and A / Case B)			
Resistance	R	50 /60/20	Ω
Inductance	L	0.34/4.4/1.5	mH
Capacitance	C	0.01/15/1	nF
Simulation parameters			
Time step	Δt	1.6×10^{-11}	s
Cell size	$\Delta x = \Delta y$	1.6×10^{-4}	m
Number of cells	$x_{\max} \times y_{\max}$	250×63 or 255	(-)
Initial number of particles per cell	N/NG	400	particles/cell
Number of iterations between outputs	N_a	5000	(-)
Permittivity scaling	α^0	64	(-)

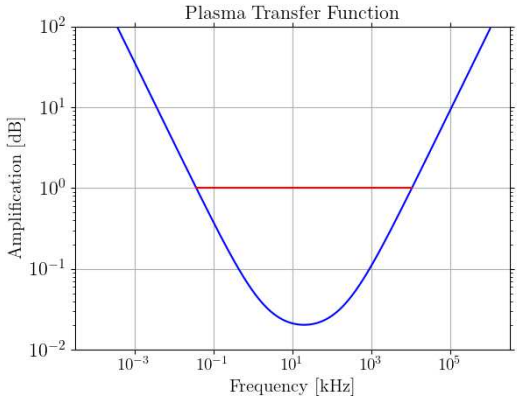

FIG. 3: Bode diagram representing Eq. 5 using the chosen circuit parameters: $R = 60\,\Omega$, $L = 4.4\,\text{mH}$ and $C = 15\,\text{nF}$.

periodic and contains strong gradients. As a consequence, an FFT analysis does not allow to distinguish how the local conditions impact the modes propagating in the axial direction. In order to overcome this issue, it is possible to use a power spectral density (PSD) reconstruction technique named two-point power spectral density method (PSD2P). This technique is based on the works by Beall *et al.*[40] and by Dudok de Wit *et al.*[41] and allows to calculate 2D wavenumber-frequency dispersion maps by studying the correlation of the signal (the electron density in our case) between two different points of the simulation. In more recent years, other methods have been developed to better resolve the 2D modes, among them MUSIC (MUltiple SIgnal Classification)[47] has been successfully used to obtain the time-space spectrum[48]. However, in the current work we chose to focus only on the PSD2P, in particular because it allows to derive some information on the amplitude of the mode. By using this method, the reconstruction of the PSD is obtained in a very localized position of the simulation, as compared to a standard FFT. The impact of the local plasma parameters in the axial modes can then be revealed even during a BM oscillation where strong axial gradients are present. In the next section, we describe concisely the technique developed by Beall *et al.*[40]. The reader can refer to this reference for more details.

A. PSD2P Technique description

To compute the spectrum along the axial direction, let us consider two probes at a fixed azimuthal position and at axial positions $x = x_1$ and $x = x_2$, and let χ_p be the distance between them. Then take M pairs (x_1, x_2) along the azimuthal direction, one at every grid point. The PSD2P is applied on a time interval T, corresponding to N timesteps, with $\Delta t = T/N$. The temporal signal is recorded and is noted $B^{(j)}(x_i, t)$, with $i = 1, 2$, and the superscript refers to the j^{th} pair. This signal is multiplied by the Hamming windowing function, and its spectral components are calculated thanks to a discrete Fourier transform (DFT), as

$$B^{(j)}(x_i, \omega) = \frac{1}{N} \sum_{l=1}^{N} B_w^{(j)}(x_i, l\Delta t) \exp(-\imath \omega l \Delta t).$$

Here, the subscript w stands for *windowed* and the unit imaginary number $\imath = \sqrt{-1}$. The frequencies used to decompose the signal are computed as a function of the time step, as follows,

$$\omega = \left[-\frac{N}{2}, ..., -1,\ 0,\ 1, ..., \frac{N}{2} - 1 \right] \cdot \frac{2\pi}{T}.$$

For each pair of points and for each frequency, we write the sample cross spectrum as

$$H^{(j)}(\omega, \chi_p) = B^{(j)*}(x_1, \omega) B^{(j)}(x_2, \omega) = C^{(j)}(\omega) + \imath Q^{(j)}(\omega), \tag{6}$$

where the star indicates the complex conjugate. We construct a matrix of local wavenumbers, $k_p^{(j)}(\omega) = \Theta^{(j)}/\chi_p$, where the angle is given by $\Theta^{(j)} = \arctan[Q^{(j)}(\omega)/C^{(j)}(\omega)]$. Similarly to Eq. (6), we can calculate the signal self-correlation for each point of each pair, as

$$S_i^{(j)}(\omega) = H^{(j)}(\omega, \chi_p = 0) = B^{(j)*}(x_i, \omega) B^{(j)}(x_i, \omega),$$

for $i = 1, 2$. Finally, the local power spectrum can be obtained performing an ensemble average on the M pairs of points weighted by the self-correlation,

$$\hat{S}_l(k_x, \omega) = \frac{1}{M} \sum_{j=1}^{M} I_{[0,\Delta k)} \left(k_x - k_p^{(j)}(\omega) \right) \cdot \frac{1}{2} \left[S_1^{(j)}(\omega) + S_2^{(j)}(\omega) \right],$$

where $I_{[0,\Delta k)}(k_x)$ is an indicator function in the wavenumber space. In the present work the wavenumber are discretized as a function of the time step and the distance between the two points, as follows,

$$k_x = \left[-\frac{N}{4}, ..., -1,\ 0,\ 1, ..., \frac{N}{4} - 1 \right] \cdot \frac{2\pi}{\chi_p}. \tag{7}$$

Other wavenumber discretizations are also allowed by this technique but not discussed in this paper. As it can be inferred from (7), with this method we can regularly detect the instability in a fixed range $[k_{\min}, k_{\max}]$, where $k_{\max}$ and $k_{\min}$ are the boundaries of the reconstruction axis. Whenever an instability has a wavenumber $\tilde{k}$ out of this range, the instability will appear on the map at a wavenumber $\tilde{k}^* \in [k_{\min}, k_{\max}]$, such that $\tilde{k}^* = \tilde{k} - n \cdot (k_{\max} - k_{\min})$ if $\tilde{k} > 0$ and $\tilde{k}^* = \tilde{k} + n \cdot (k_{\max} - k_{\min})$ if $\tilde{k} < 0$, with $n \in \mathbb{N}^+$. This technique can also be used to compute the spectrum in the azimuthal direction, with pairs (y_1, y_2) at fixed axial position.

Electron density fluctuations have been used rather than the commonly used electric field fluctuations. This is because the magnitude of a scalar quantity is preferable when one wants to study the DRs along two different directions. In particular, we noticed that using the azimuthal electric field gave noisier spectral maps when the electric field instability direction is not aligned with the PSD2P direction. Dudok de Wit *et al.*[41] developed an interesting variant of the method described above, using wavelet transforms and time averaging on a single pair of experimental points. This method is computationally more expensive but it is more appropriate whenever one wants to calculate the spectrum using a small number of pairs (x_1, x_2), or even a single one.

V. RESULTS

A. 2D PIC axial-azimuthal simulations

1. *Simulations with a small azimuthal length,* $L_y = 1\,\mathrm{cm}$

We first study 2D PIC axial-azimuthal simulations with a reduced azimuthal length, $L_y = 1\,\mathrm{cm}$ with parameters given in Table I. Fig. 4 shows the time evolution of the discharge current and the anode potential for a base case without circuit, and for two different cases with RLC circuits discussed in Section III: case 1 is for standard HT circuit components ($R = 50\,\Omega$, $L = 340\,\mu\mathrm{H}$ and $C = 10\,\mu\mathrm{F}$); case 2 is for the optimized set of parameters ($R = 60\,\Omega$, $L = 4.4\,\mathrm{mH}$ and $C = 15\,\mathrm{nF}$).

As seen in Figure 4 (a) a quasi-steady state is reached after $\approx 100\,\mu\mathrm{s}$ and the average current at steady state is about the same for all three cases ($I_d^{mean} \simeq 3.3\,\mathrm{A}$). The circuit effect is nonetheless significant. For the base case (without circuit) the standard deviation of the current after the transient phase is $\approx 0.58\,\mathrm{A}$, and this quantity decreases to $\approx 0.46\,\mathrm{A}$ for Case 1. The BM oscillations are severely damped for Case 2, i.e. with the optimized circuit (the current standard deviation drops to $\approx 0.23\,\mathrm{A}$). The filter has almost no impact on an higher frequency oscillation (at $\approx 200\,\mathrm{kHz}$) that

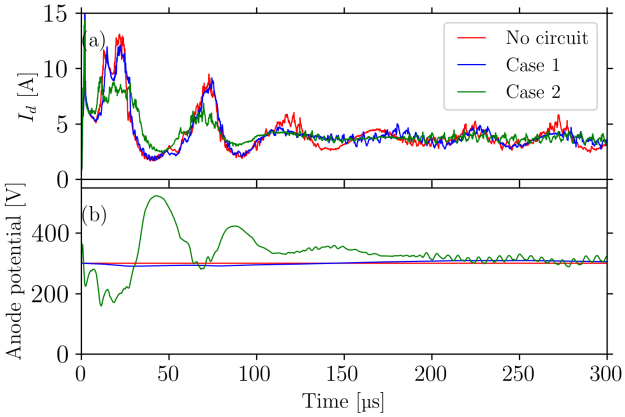

FIG. 4: Time evolution of the discharge current (a) and the anode potential (b) in 2D PIC axial-azimuthal simulations with an azimuthal length, $L_y = 1\,\text{cm}$ without *RLC* circuit, and with two different *RLC* circuits: case 1 is for standard HT circuit components ($R = 50\,\Omega$, $L = 340\,\mu\text{H}$ and $C = 10\,\mu\text{F}$); case 2 is for the optimized set of parameters ($R = 60\,\Omega$, $L = 4.4\,\text{mH}$ and $C = 15\,\text{nF}$).

is observed in all three cases. In Figure 4 (b) we observe that the anode voltage varies significantly during the first BM periods with the optimized circuit, while for case 1 the voltage variation is negligible (without circuit the anode voltage is constant). This study shows that the use of an optimized *RLC* circuit can completely damp the BM oscillations in cases where the standard deviation of the oscillations is small and, hence, close to a linear regime.

2. *Simulations with a larger azimuthal length,* $L_y = 4\,\text{cm}$

We now run simulations with a larger azimuthal lenght, $L_y = 4\,\text{cm}$, and we also investigate the effect of the temperature of electrons injected at the cathode boundary. Figure 5 shows the time evolution of the discharge current and the anode potential, without *RLC* circuit, and with an optimized *RLC* circuit for two values of the temperature of the electrons emitted from the cathode: Case A with $T_e^{cath} = 5\,\text{eV}$, $R = 60\,\Omega$, $L = 4.4\,\text{mH}$ and $C = 15\,\text{nF}$, Case B with $T_e^{cath} = 0.1\,\text{eV}$, $R = 20\,\Omega$, $L = 1.5\,\text{mH}$ and $C = 1\,\text{nF}$. These two different sets of circuit parameters are designed

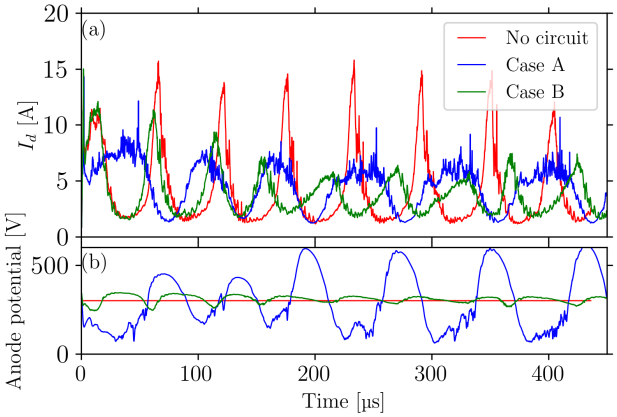

FIG. 5: Time evolution of the discharge current (a) and the potential (b) in 2D PIC axial-azimuthal simulations with an azimuthal length, $L_y = 4\,\mathrm{cm}$ without *RLC* circuit, and for a *RLC* circuit with an optimized set of parameters for two values of the temperature of the electrons emitted from the cathode: Case A with $T_e^{cath} = 5\,\mathrm{eV}$, Case B with $T_e^{cath} = 0.1\,\mathrm{eV}$.

to damp the BM oscillation with a very similar circuit response (calculated via Eq. (4)), but with a different time constants (i.e. $\tau \propto 1/\sqrt{LC}$), such that $\tau_A < \tau_B$). First, we observe that without *RLC* circuit the frequency of the BM is similar to that of the small $L_y = 1\,\mathrm{cm}$ case (see Figure 4). However, as observed in Charoy *et al.*[24], the amplitude of the fluctuations increases dramatically (it is 5 to 10 times larger for $L_y = 4\,\mathrm{cm}$ than for $L_y = 1\,\mathrm{cm}$). As already mentioned, such large fluctuations have severe numerical consequences: (i) the PIC requirements may be violated near the peak (λ_D and ω_{pe} both depend on the plasma density), and/or (ii) the computational cost of each simulation becomes unrealistic, and (iii) the high current peaks are followed by low current phases during which the extinction of the discharge may occur. Therefore, the use of the *RLC* circuit is crucial to run simulations with an azimuthal domain length of several centimeters.

With an optimized *RLC* circuit and a temperature of emitted electrons of 5 eV (similar to that in Figure 4), we observe in Figure 5 Case A that the circuit does not allow to completely damp the oscillations for $L_y = 4\,\mathrm{cm}$. Nevertheless, the circuit is able to successfully prevents the large unphysical fluctuations that were otherwise observed.

The temperature of the electrons emitted from the cathode depends on the cathode device and

may vary in time. In most axial-azimuthal PIC simulations, it has been traditionally fixed to a constant value ($T_e^{cath} = 5\,\mathrm{eV}$ in the cases described heretofore). Without *RLC* circuit, Charoy[12] observed that the choice of the cathode temperature affects the discharge behavior. For this reason, we investigated the results obtained with a *RLC* circuit for two different cases: Case A with $T_e^{cath} = 5\,\mathrm{eV}$, the usual choice, and Case B with lower $T_e^{cath} = 0.1\,\mathrm{eV}$. In Figure 5 we observe that the effect on the discharge current waveform is limited, but with smaller current oscillations and higher frequency for case B. However, we observe a significant difference in the anode voltage: in case B the circuit response is slower and the anode voltage barely oscillates, while in case A the circuit response is faster and the anode voltage oscillations are large.

The fact that the BM is present for the $L_y = 4\,\mathrm{cm}$ cases, while it is almost perfectly damped for the $L_y = 1\,\mathrm{cm}$ cases (i.e. Case 2), supports the idea that the simulations with small L_y do not capture all the discharge physics complexity, and more precisely the influence of the azimuthal modes on the axial modes.

In Figures 6 and 7 we plot the time evolution of the discharge current in cases A and B, respectively, with the axial profiles of electron temperature and density at different times during the BM period. First, we note that the BM frequency decreases when we use a lower injection temperature at the cathode. More importantly, in Case A there is a strong high-frequency oscillation that is absent in Case B. The axial profiles of electron temperature and density at different times in Figures 6 and 7 show that the plasma parameters oscillate more in the case of an higher injection temperature. The electron temperature profiles are however fairly similar in both cases. We observe that the temperature is higher in the decreasing BM phase, with a maximum at the channel exit (i.e. between 2 and 2.5 cm). The profiles show strong inhomogeneities in the axial direction, justifying the need of PSD2P to compute the fluctuations spectra along this direction. In the bottom row of Figures 6 and 7 we observe the axial profile of the cyclotron frequency ω_{ce}, of the anomalous collision frequency ν_t and of the classical collision frequency ν_{class}. The anomalous collision frequency is calculated from the electron mobility in axial direction as

$$\mu_{e,x} = \frac{v_{e,x}}{E_x + \nabla(n_e k_b T_e)/n_e e},$$

by the usual mobility formula for magnetized plasmas: $\nu_e = m_e \omega_{ce}^2 \mu_{e,x}/e$. In both cases A and B, the profile of ν_t is rather smooth in the thruster channel, while it is more noisy in the plume. This fact is related to the method of calculation of the mobility. Dale *et al.*[49] propose a similar graph in an experimental work. In particular, they observe that the classical collision frequency

decreases from the mid-channel to the first centimeters of the plume, while the anomalous collisional frequency increases: this is what we observe here. Interestingly, we find the same trends and a similar order of magnitude for all the quantities. The differences are probably related to the different conditions of their discharge.

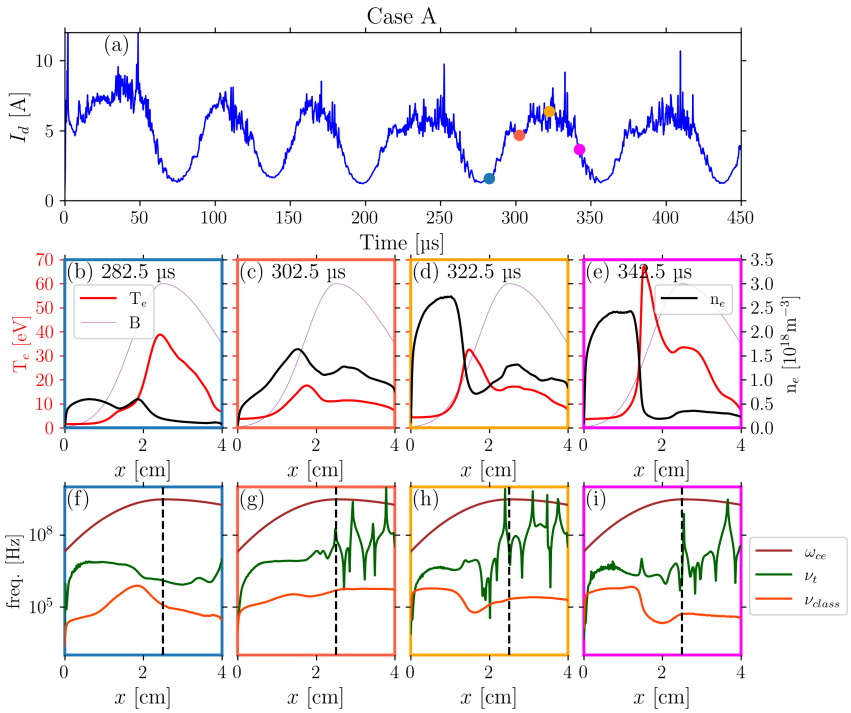

FIG. 6: **Case A** with $T_e^{cath} = 5\,\text{eV}$. (a) The discharge current. The four points indicates the times at which the profiles in (b-e) and (f-i) are taken (the marker color corresponds to the frame color in the bottom line). In the central line panels we show the axial profiles of electron temperature (red) and electron density (black) at the chosen times. The purple line represents the magnetic field profile in linear scale. In the bottom panels we show the axial profiles of the cyclotron frequency ω_{ce}, the anomalous collisional frequency ν_t and of the classical collisional frequency ν_{class}. The dashed black line represents the thruster exit plan.

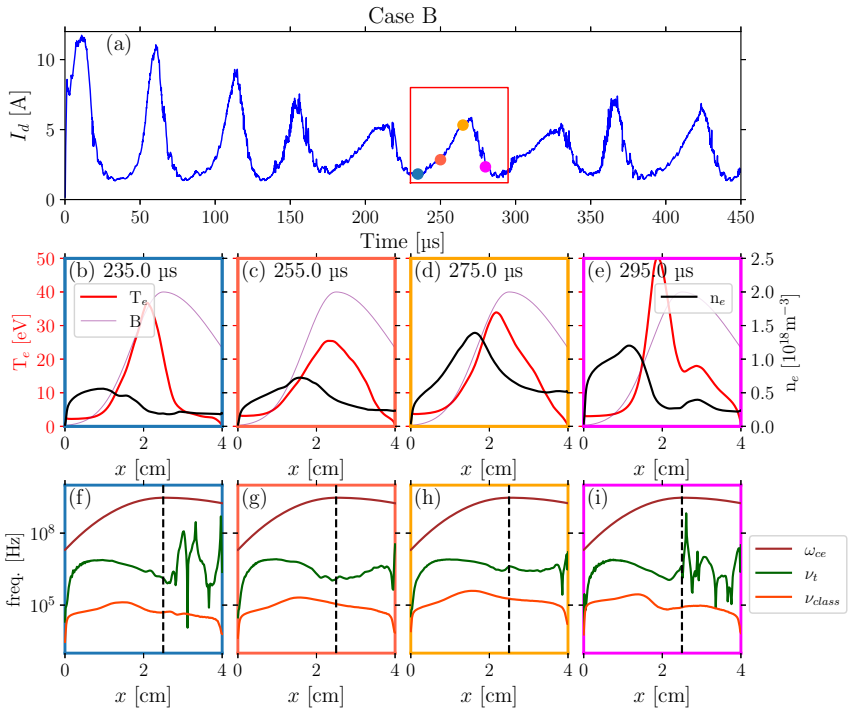

FIG. 7: **Case B** with $T_e^{cath} = 0.1\,\text{eV}$. (a) The discharge current. The four points indicates the times at which the profiles in (b-e) and (f-i) are taken (the marker color corresponds to the frame color in the bottom line). In the central line panels we show the axial profiles of electron temperature (red) and electron density (black) at the chosen times. The purple line represents the magnetic field profile in linear scale. In the bottom panels we show the axial profiles of the cyclotron frequency ω_{ce}, the anomalous collisional frequency ν_t and of the classical collisional frequency ν_{class}. The dashed black line represents the thruster exit plan.

B. PSD2P method for 2D axial-azimuthal PIC simulations analysis

In this section, we use the PSD2P method to analyze the instability spectra in cases A and B (i.e. 2D axial-azimuthal simulations with a $4\,\mathrm{cm} \times 4\,\mathrm{cm}$ domain with an optimized *RLC* circuit) described in the previous section. As reported in Charoy *et al.*[24], the time evolution of the plasma discharge during a BM oscillation can be separated in two stages: the growing phase of the BM, where the dominant instabilities are the high-frequency mainly-azimuthal ECDI/IAW, and the decreasing phase of the BM where the intermediate frequency axial ITTI dominates. The spectra are generated both in the azimuthal and in the axial directions, which allows to accurately determine the direction of the propagation of the various modes. This analysis of the direction of the propagation will be detailed further in Paper II, where we will analyze thoroughly the amplitude evolution of the spectra along the thruster axis.

First, to validate the results obtained by the PSD2P method, we have compared the spectrum in the azimuthal direction as computed by a standard FFT and by a PSD2P reconstruction. In Fig. 8 we show an example of the spectrum calculated from the PIC electron density signal extracted from the plume of Case B (at $x = 3.41\,\mathrm{cm}$) at $t = 262\,\mu\mathrm{s}$. A standard Fast Fourier Transform (FFT) map is shown in Fig. 8 (a) while a PSD2P map is shown in Fig. 8 (b). Both techniques are able to detect the modes with maximum amplitude, that correspond to $\omega \approx 1\,\mathrm{MHz}$ and $k_y \approx 500\ \mathrm{m}^{-1}$. However, we can see that the PSD2P is able to capture the spectrum with higher resolution in both the wavenumber and the frequency.

In Figures 9, 11, 10 and 12 we present several PSD2P maps, calculated for Cases A and B, both in axial and azimuthal directions. In particular, we calculate the PSD2P in the growing phase of the BM in Figs 9 and 10 and in the decreasing phase of the BM in Figs 11 and 12.

1. *Analysis during the growing phase of the BM*

We present PSD2P maps during the growing phase of a BM oscillation in Figures 9 (Case A) and 10 (Case B). In both cases, we analyze both the axial and the azimuthal spectrum in two different points of the thruster, one inside the channel and one in the plume. In addition, we select the mode at high-frequency with large amplitudes and we plot the direction of propagation.

As observed by Charoy *et al.*[24], the spectrum is dominated by the ECDI/IAW during the growing phase. We can distinguish two regions: one close to the anode, where the instability propagates

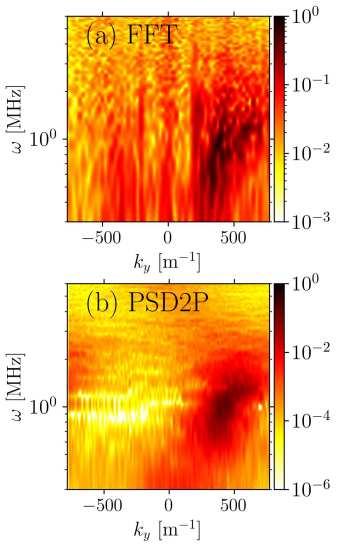

FIG. 8: Spectrum in the azimuthal direction calculated from the PIC electron density signal extracted from the plume of Case B (at $x = 3.41$ cm) at $t = 262\,\mu$s: Spectrum obtained using a 2D FFT technique in (a) and with the PSD2P technique in (b). The PIC signal analyzed is the electron density fluctuations at a fixed axial position for a time interval of 8 µs. The low resolution of the FFT is related to the fact that we used a standard 2D dimensional FFT.

at a finite angle with respect to the azimuthal direction, and one in the plume, where the propagation is essentially in the azimuthal direction. Inside the channel, plotted in subfigures 9 and 10 (a) and (d), we observe that there are only small differences between Cases A and B. In both cases, we observe that the instability propagates with a significant angle, with an inclination of the wave vector towards the anode, as shown by the cyan arrows in Figures 9 and 10 (c). The most significant differences between Case A and Case B appear in the plasma plume, in the PSD2P maps of subfigures 9 and 10 (b) and (e). In Case B Figure 10(e), we clearly identify the frequency and wavenumber corresponding to the ECDI at $\omega \approx 1\,$MHz and $k_y \approx 400\,\mathrm{m}^{-1}$, while the spectrum in Figure 9(e) calculated for Case A is more complex. The signature of the ECDI at high frequency and wavenumber is still seen, but the main mode is at lower frequency and wavenumber, within

the range reported in Section II A for the ITTI. It therefore appears that the PSD2P technique is able to capture the simultaneous presence of both modes.

As it can be seen in Figure 10 (b), the ECDI/IAW also has a signature in the axial direction. The mode with the largest amplitude is seen at $k_x = 0$. As a result, we observe a wave that propagates almost azimuthally. However, the axial dispersion map, that was not analyzed in previous works, suggests that the ECDI/IAW may have a 2D nature. The spectrum is broad, and can be compared to the the theoretical IAW dispersion relation, as already done in several works[16,24,27,42,46,50]. This discussion about the 2D nature of the IAW and the comparison with the analytical DR will be carried out in Paper II.

In Figures 9 and 10 we observe that the PSD2P technique successfully captures the bending of the wavefronts, observed in the density snapshots. In addition, we observe a change of frequency of the dominant ECDI/IAW mode between the region near the anode and that near the thruster exit. These results are consistent with the change of direction in the propagation of the wave and change of frequency along the thruster axis as observed by Ben Slimane *et al.*[50] using virtual Thomson scattering. This will be further discussed in Paper II.

2. *Analysis in the decreasing phase of the BM*

The PSD2P maps of the decreasing phase of the discharge current are shown in Figures 11 and 12 for cases A and B, respectively. As already observed by Charoy *et al.*[24], the spectrum and dynamics of the instabilities is very different to that in the growing phase. In the thruster channel we still observe an ECDI-like instability that propagates at a finite angle with respect to the thruster axis, but the spectrum in the plume changes drastically. In this region we observe a longer-wavelength instability, directed mainly axially, identifiable as the ITTI. This instability, which has a frequency of the order of 500 kHz and a wavelength of the order of 1 cm, is also captured in the dispersion maps by the PSD2P technique. Its frequency in Case A is of ≈ 600 kHz and in Case B of ≈ 300 kHz, while the axial wavenumbers are $\approx 80\,\mathrm{m}^{-1}$ and $\approx 40\,\mathrm{m}^{-1}$, respectively. In the axial PSD2P map, we observe that the instability dispersion has approximately the same shape as the resistive mode identified by Fernandez *et al.*[21] in radial-axial simulations. A complete comparison between the linear theory and the PSD2P spectra is presented in Paper II.

Even if the azimuthal PSD peak remains at $k_y \approx 0$, we observe that the PSD2P map is not perfectly symmetric. In particular, we note in Figure 11 (e) that the azimuthal wavenumber is not

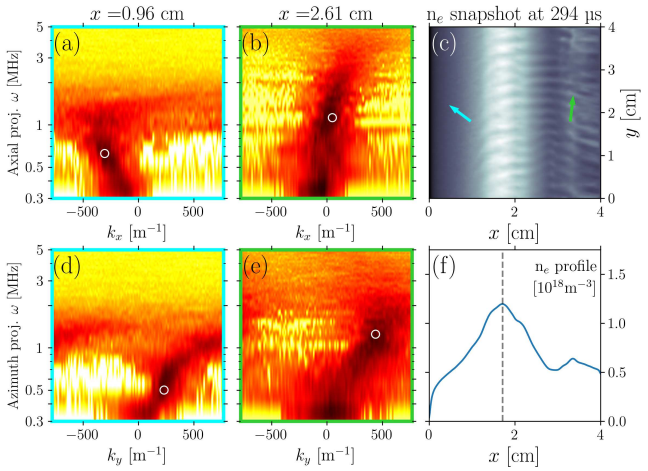

FIG. 9: **Case A, growing phase of the BM**. In (a) and (b): PSD2P maps calculated in the axial direction in the channel and in the plume. In (d) and (e): PSD2P maps calculated in the azimuthal direction at the same axial positions. The white rings represent the max of the PSD2P. In (c): snapshot of the electron density map at $t = 294\,\mu$s. The arrows represent the instability direction, that is calculated by the k_x and k_y in the spectra. Each frame corresponds to the arrow with the same color. In (f): axial profile of the electron density at $t = 294\,\mu$s.

perfectly centered at zero, as one would expect for a perfectly axial instability. This is a hint that the ITTI may have a small azimuthal component. It will be shown in Paper II that this observation is crucial to understand the linear phase growth of this instability.

3. Analysis over the entire BM period

The comparison of the spectra of Cases A and B during an entire BM period suggests the following. In Case A, the ITTI is present in both phases and is dominant in the plume during the phase of discharge current collapse. In Case B, two different dispersion maps are identified: one dominated by ECDI/IAW with almost no ITTI during the growing phase of the discharge current (i.e. in Figure 10, the instability in the plume is purely azimuthal), and another one dominated by the ITTI with almost no presence of ECDI/IAW in the plume during the decreasing phase of the discharge current. As further discussed in paper II, the origin of this difference may be explained

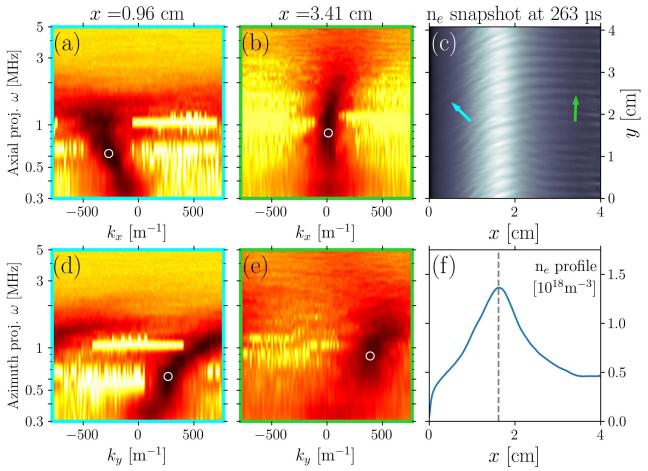

FIG. 10: **Case B, growing phase of the BM**. In (a) and (b): PSD2P maps calculated in the axial direction in the channel and in the plume. In (d) and (e): PSD2P maps calculated in the azimuthal direction at the same axial positions. The white rings represent the max of the PSD2P. In (c): snapshot of the electron density map at $t = 263\,\mu s$. The arrows represent the instability direction, that is calculated by the k_x and k_y in the spectra. Each frame corresponds to the arrow with the same color. In (f) axial profile of the electron density at $t = 263\,\mu s$.

by the ITTI growth rate derived from fluid theory, which depends on the collision frequency[21], so on the electron temperature (the plume electron temperature is different in cases A and B).

VI. CONCLUSION AND FURTHER DISCUSSIONS

In this work we have analyzed instabilities in $\mathbf{E} \times \mathbf{B}$ discharges of typical HT configurations based on the results obtained with 2D PIC-MCC axial-azimuthal simulations. The understanding of these instabilities is of primary importance because they impact the discharge physics and the thruster efficiency[7]. One of the dominant modes that develops in HTs is the BM, a low-frequency instability ($\approx 10\,kHz$) that is related to the ionization of the neutral gas. In order to capture several periods of this mode and reach a quasi-stationary state with a PIC simulation, very long simulations are needed ($\approx 500\,\mu s$ of physical time) with a computational cost of the order of weeks on thousands of CPUs. For this reason, we have used a scaling technique that consists in artificially

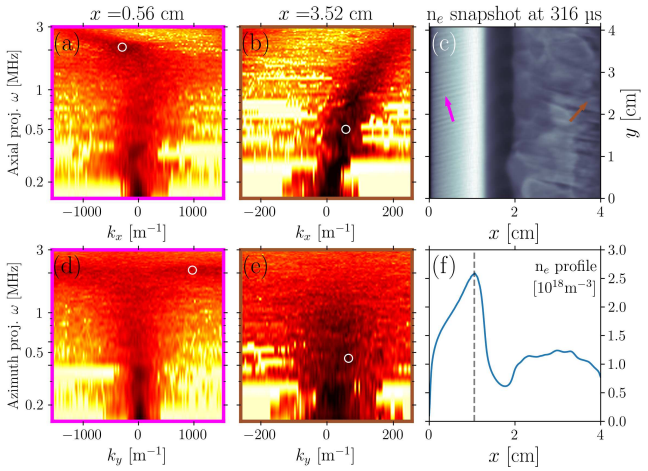

FIG. 11: **Case A, decreasing phase of the BM**. In (a) and (b) we show the PSD2P calculated in the axial direction in the channel and in the plume. In (d) and (e) we show the the PSD2P calculated in the azimuthal direction at the same axial positions. The maximal density is very close to $x = 0.96$ cm (i.e. the axial position chosen for the other figures), so we performed the analysis at position slightly closer to the anode. The white rings represent the max of the PSD2P. In (c) a snapshot of the electron density map at $t = 316$ µs is shown. The arrows represent the instability direction, that is calculated by the k_x and k_y in the spectra. Each frame corresponds to the arrow with the same color. In (f) we report the electron density axial profile at $t = 316$ µs.

increasing the vacuum permittivity[30,38], which relaxes the numerical constraints of the PIC simulations. However, the artificial permittivity has an impact on the growth rate of the electrostatic instabilities, and it also increases artificially the wavelength of certain modes. For this reason, the azimuthal length used in this work ($L_y = 4$ cm) is larger than the typical length used in previous axial-azimuthal PIC simulations[36,37].

It was previously observed that without ballast or filter, the BM oscillations may become extremely large, and may even drive the discharge into unphysical conditions[24,34]. In this work, this problem is overcome by using an external *RLC* circuit[39] that strongly damps the discharge current oscillations. Such circuits are also used in experiments.

The study of plasma instabilities is an extremely active field in the $\mathbf{E} \times \mathbf{B}$ community[3]. How-

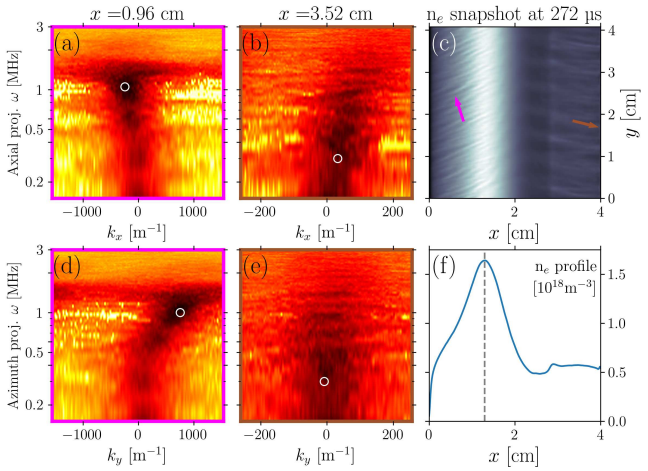

FIG. 12: **Case B, decreasing phase of the BM**. In (a) and (b) we show the PSD2P calculated in the axial direction in the channel and in the plume. In (d) and (e) we show the the PSD2P calculated in the azimuthal direction at the same axial positions. The white rings represent the max of the PSD2P. In (c) a snapshot of the electron density map at $t = 272\,\mu s$ is shown. The arrows represent the instability direction, that is calculated by the k_x and k_y in the spectra. Each frame corresponds to the arrow with the same color. In (f) we report the electron density axial profile at at $t = 272\,\mu s$.

ever, despite the extensive literature about the azimuthal instabilities[5,6,11,25,28,31], there are only few studies[21,50] of the axial modes. The origin of this difference may be related to the difficulty of calculating a spectrum in the axial direction, in which strong gradients are present. In this paper, it was shown that by using the PSD2P method, developed by Beall *et al.*[40], it is possible to successfully construct the PSD spectrum at a given axial position. In Paper II this powerful technique will be coupled to a theoretical derivation of fluid 3D dispersion relations for electrostatic instabilities $\mathbf{E} \times \mathbf{B}$ discharges.

The effect of different electron cathode injection temperatures, at $T_e^{cath} = 5\,eV$ and $T_e^{cath} = 0.1\,eV$, was also investigated. In agreement with Ref.[34], we observe that the cathode temperature affects the discharge dynamics (i.e. the BM amplitude and period). Here the impact of the injection in the electrostatic modes was demonstrated by using the PSD2P reconstruction. It was shown that

the same electrostatic instabilities develop in the two cases: the ECDI/IAW during the growing phase of the BM and the ITTI during the decreasing one. However, different cathode injection temperatures induce significant differences to the ITTI growth. Larger injection temperatures lead to larger ITTI fluctuations, that remain active over the whole BM cycle, while with lower injection temperatures, fluctuations are smaller and almost disappear during the growing phase of the BM .

Both ECDI/IAW and ITTI instabilities have a dominant propagation direction (azimuthal for the ECDI/IAW and axial for the ITTI). However, thanks to the PSD2P technique, the two-dimensional character of these instabilities, that heretofore have been seen as mono-dimensional instabilities, has been clearly demonstrated. In Paper II we will analyse in detail the 2D effects on the instabilities growth and propagation, and it will be shown that 2D effects are very important.

ACKNOWLEDGMENTS

FP acknowledges financial support from a Safran Aircraft Engines doctoral research award as well as from the Association Nationale de la Recherche et de la Technologie (ANRT) as part of a CIFRE convention. This work has been partially funded by ANR (n^{o} ANR-16-CHIN-003-01) and Safran Aircraft Engines with the project POSEIDON. This work was granted access to the HPC resources of CINES under the allocations A0100510439 and A0120510439 made by GENCI.

DATA AVAILABILITY

The data that support the findings of this study are available from the corresponding author upon reasonable request.

REFERENCES

[1]A. I. Morozov and V. V. Savelyev, FUNDAMENTALS OF STATIONARY PLASMA THRUSTER THEORY (Springer, 2000).

[2]D. M. Goebel and I. Katz, Fundamentals of Electric Propulsion: Ion and Hall Thrusters, JPL SPACE SCIENCE AND TECHNOLOGY SERIES (Wiley, 2008).

[3]I. D. Kaganovich, A. Smolyakov, Y. Raitses, E. Ahedo, I. G. Mikellides, B. Jorns, F. Taccogna, R. Gueroult, S. Tsikata, A. Bourdon, J.-P. Boeuf, M. Keidar, A. T. Powis, M. Merino, M. Cappelli, K. Hara, J. A. Carlsson, N. J. Fisch, P. Chabert, I. Schweigert, T. Lafleur, K. Matyash, A. V. Khrabrov, R. W. Boswell, and A. Fruchtman, "Physics of E B discharges relevant to plasma propulsion and similar technologies," Physics of Plasmas **27**, 120601 (2020).

[4]P. Kelly and R. Arnell, "Magnetron sputtering: a review of recent developments and applications," Vacuum **56**, 159–172 (2000).

[5]A. Ducrocq, J. C. Adam, A. Héron, and G. Laval, "High-frequency electron drift instability in the cross-field configuration of Hall thrusters," Physics of Plasmas **13**, 102111 (2006).

[6]J. Cavalier, N. Lemoine, G. Bonhomme, S. Tsikata, C. Honoré, and D. Grésillon, "Hall thruster plasma fluctuations identified as the EB electron drift instability: Modeling and fitting on experimental data," Physics of Plasmas **20**, 082107 (2013).

[7]T. Lafleur, S. D. Baalrud, and P. Chabert, "Theory for the anomalous electron transport in Hall effect thrusters. II. Kinetic model," Physics of Plasmas **23**, 053503 (2016).

[8]T. Lafleur, S. D. Baalrud, and P. Chabert, "Theory for the anomalous electron transport in Hall effect thrusters. I. Insights from particle-in-cell simulations," Physics of Plasmas **23**, 053502 (2016).

[9]O. Koshkarov, A. Smolyakov, Y. Raitses, and I. Kaganovich, "Self-Organization, Structures, and Anomalous Transport in Turbulent Partially Magnetized Plasmas with Crossed Electric and Magnetic Fields," Physical Review Letters **122**, 185001 (2019).

[10]J.-P. Boeuf, "Tutorial: Physics and modeling of Hall thrusters," Journal of Applied Physics **121**, 011101 (2017).

[11]K. Hara, "An overview of discharge plasma modeling for Hall effect thrusters," Plasma Sources Science and Technology **28**, 044001 (2019).

[12]T. Charoy, T. Lafleur, A. Tavant, P. Chabert, and A. Bourdon, "A comparison between kinetic theory and particle-in-cell simulations of anomalous electron transport in E B plasma

discharges," Physics of Plasmas **27**, 063510 (2020).

[13]S. Tsikata and T. Minea, "Modulated Electron Cyclotron Drift Instability in a High-Power Pulsed Magnetron Discharge," Physical Review Letters **114**, 185001 (2015).

[14]J. C. Adam, J. P. Boeuf, N. Dubuit, M. Dudeck, L. Garrigues, D. Gresillon, A. Heron, G. J. M. Hagelaar, V. Kulaev, N. Lemoine, S. Mazouffre, J. Perez Luna, V. Pisarev, and S. Tsikata, "Physics, simulation and diagnostics of Hall effect thrusters," Plasma Physics and Controlled Fusion **50**, 124041 (2008).

[15]J. C. Adam, A. Héron, and G. Laval, "Study of stationary plasma thrusters using two-dimensional fully kinetic simulations," Phys. Plasmas **11**, 12 (2004).

[16]T. Lafleur and P. Chabert, "The role of instability-enhanced friction on 'anomalous' electron and ion transport in Hall-effect thrusters," Plasma Sources Science and Technology **27**, 015003 (2017).

[17]K. Hara, M. J. Sekerak, I. D. Boyd, and A. D. Gallimore, "Perturbation analysis of ionization oscillations in Hall effect thrusters," Physics of Plasmas **21**, 122103 (2014).

[18]T. Lafleur, P. Chabert, and A. Bourdon, "The origin of the breathing mode in Hall thrusters and its stabilization," Journal of Applied Physics **130**, 053305 (2021).

[19]O. Chapurin, A. I. Smolyakov, G. Hagelaar, and Y. Raitses, "On the mechanism of ionization oscillations in Hall thrusters," Journal of Applied Physics **129**, 233307 (2021).

[20]V. Giannetti, M. M. Saravia, and T. Andreussi, "Measurement of the breathing mode oscillations in Hall thruster plasmas with a fast-diving triple Langmuir probe," Physics of Plasmas **27**, 123502 (2020).

[21]E. Fernandez, M. K. Scharfe, C. A. Thomas, N. Gascon, and M. A. Cappelli, "Growth of resistive instabilities in EB plasma discharge simulations," Physics of Plasmas **15**, 012102 (2008).

[22]S. Barral, K. Makowski, Z. Peradzyński, and M. Dudeck, "Transit-time instability in Hall thrusters," Physics of Plasmas **12**, 073504 (2005).

[23]G. J. M. Hagelaar, J. Bareilles, L. Garrigues, and J.-P. Boeuf, "Role of anomalous electron transport in a stationary plasma thruster simulation," Journal of Applied Physics **93**, 67–75 (2003).

[24]T. Charoy, T. Lafleur, A. A. Laguna, A. Bourdon, and P. Chabert, "The interaction between ion transit-time and electron drift instabilities and their effect on anomalous electron transport in Hall thrusters," Plasma Sources Science and Technology **30**, 065017 (2021).

[25]S. Janhunen, A. Smolyakov, D. Sydorenko, M. Jimenez, I. Kaganovich, and Y. Raitses, "Evolution of the electron cyclotron drift instability in two-dimensions," Physics of Plasmas **25**, 082308

(2018).

[26]I. G. Mikellides and A. L. Ortega, "Growth of the modified two-stream instability in the plume of a magnetically shielded Hall thruster," Physics of Plasmas **27**, 100701 (2020).

[27]F. Petronio, A. Tavant, T. Charoy, A. Alvarez Laguna, A. Bourdon, and P. Chabert, "Conditions of appearance and dynamics of the modified two-stream instability in E B discharges," Physics of Plasmas **28**, 043504 (2021).

[28]W. Villafana, F. Petronio, A. C. Denig, M. J. Jimenez, D. Eremin, L. Garrigues, F. Taccogna, A. Alvarez-Laguna, J. P. Boeuf, A. Bourdon, P. Chabert, T. Charoy, B. Cuenot, K. Hara, F. Pechereau, A. Smolyakov, D. Sydorenko, A. Tavant, and O. Vermorel, "2D radial-azimuthal particle-in-cell benchmark for E B discharges," Plasma Sources Science and Technology **30**, 075002 (2021).

[29]A. Héron and J. C. Adam, "Anomalous conductivity in Hall thrusters: Effects of the non-linear coupling of the electron-cyclotron drift instability with secondary electron emission of the walls," Physics of Plasmas **20**, 082313 (2013).

[30]P. Coche and L. Garrigues, "A two-dimensional (azimuthal-axial) particle-in-cell model of a Hall thruster," Physics of Plasmas **21**, 023503 (2014).

[31]T. Lafleur, R. Martorelli, P. Chabert, and A. Bourdon, "Anomalous electron transport in Hall-effect thrusters: Comparison between quasi-linear kinetic theory and particle-in-cell simulations," Physics of Plasmas **25**, 061202 (2018).

[32]F. Taccogna and L. Garrigues, "Latest progress in Hall thrusters plasma modelling," Reviews of Modern Plasma Physics **3**, 12 (2019).

[33]L. Wang, A. Hakim, B. Srinivasan, and J. Juno, "Electron cyclotron drift instability and anomalous transport: two-fluid moment theory and modeling," arXiv:2107.09874 [physics] (2021), arXiv: 2107.09874.

[34]T. Charoy, Numerical study of electron transport in Hall thrusters, Ph.D. thesis, Ecole Polytechnique (2020).

[35]V. Croes, T. Lafleur, Z. Bonaventura, A. Bourdon, and P. Chabert, "2D particle-in-cell simulations of the electron drift instability and associated anomalous electron transport in Hall-effect thrusters," Plasma Sources Science and Technology **26**, 034001 (2017).

[36]T. Charoy, J. P. Boeuf, A. Bourdon, J. A. Carlsson, P. Chabert, B. Cuenot, D. Eremin, L. Garrigues, K. Hara, I. D. Kaganovich, A. T. Powis, A. Smolyakov, D. Sydorenko, A. Tavant, O. Vermorel, and W. Villafana, "2D axial-azimuthal particle-in-cell benchmark for low-temperature

partially magnetized plasmas," Plasma Sources Science and Technology **28**, 105010 (2019).

[37]J. P. Boeuf and L. Garrigues, "E B electron drift instability in Hall thrusters: Particle-in-cell simulations vs. theory," Physics of Plasmas **25**, 061204 (2018).

[38]H. Liu, B. Wu, D. Yu, Y. Cao, and P. Duan, "Particle-in-cell simulation of a Hall thruster," Journal of Physics D: Applied Physics **43**, 165202 (2010).

[39]S. Barral and J. Miedzik, "Numerical investigation of closed-loop control for Hall accelerators," Journal of Applied Physics **109**, 013302 (2011).

[40]J. M. Beall, Y. C. Kim, and E. J. Powers, "Estimation of wavenumber and frequency spectra using fixed probe pairs," Journal of Applied Physics **53**, 3933–3940 (1982).

[41]T. Dudok de Wit, V. V. Krasnosel'skikh, S. D. Bale, M. W. Dunlop, H. Lühr, S. J. Schwartz, and L. J. C. Woolliscroft, "Determination of dispersion relations in quasi-stationary plasma turbulence using dual satellite data," Geophysical Research Letters **22**, 2653–2656 (1995).

[42]Z. A. Brown and B. A. Jorns, "Spatial evolution of small wavelength fluctuations in a Hall Thruster," Physics of Plasmas **26**, 113504 (2019).

[43]M. M. Turner, A. Derzsi, Z. Donkó, D. Eremin, S. J. Kelly, T. Lafleur, and T. Mussenbrock, "Simulation benchmarks for low-pressure plasmas: Capacitive discharges," Physics of Plasmas **20**, 013507 (2013).

[44]E. F. Toro, Riemann solvers and numerical methods for fluid dynamics: a practical introduction, 2nd ed. (Springer-Verlag, Berlin ; New York, 1999).

[45]C. K. Birdsall and A. B. Langdon, Plasma physics via computer simulation (McGraw-Hill, New York, 1985).

[46]Z. Asadi, F. Taccogna, and M. Sharifian, "Numerical Study of Electron Cyclotron Drift Instability: Application to Hall Thruster," Frontiers in Physics **7**, 140 (2019).

[47]R. Kleiber, M. Borchardt, A. Könies, and C. Slaby, "Modern methods of signal processing applied to gyrokinetic simulations," Plasma Physics and Controlled Fusion **63**, 035017 (2021).

[48]L. Xu, D. Eremin, and R. P. Brinkmann, "Direct evidence of gradient drift instability being the origin of a rotating spoke in a crossed field plasma," Plasma Sources Science and Technology **30**, 075013 (2021).

[49]E. T. Dale and B. A. Jorns, "Non-invasive time-resolved measurements of anomalous collision frequency in a hall thruster," Physics of Plasmas **26**, 013516 (2019).

[50]T. Ben Slimane, C. Honoré, T. Charoy, A. Bourdon, and P. Chabert, "Analysis of small scale fluctuations in Hall effect thrusters using virtual Thomson scattering on PIC simulations,"

Physics of Plasmas **29**, 023501 (2022).

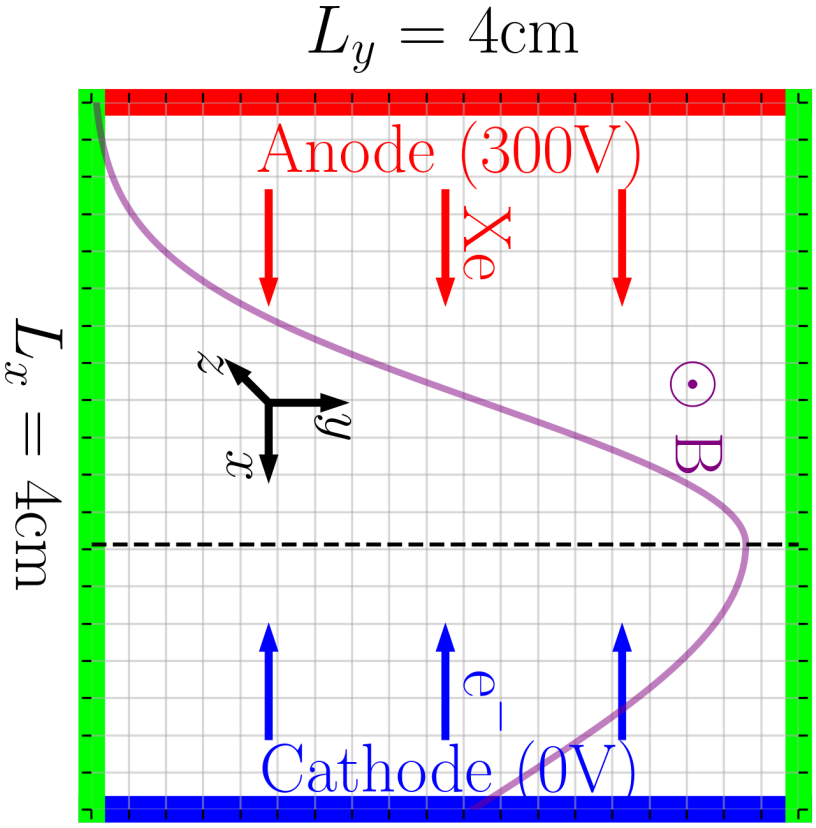

PLEASE CITE THIS ARTICLE AS DOI: 10.1063/5.0119253

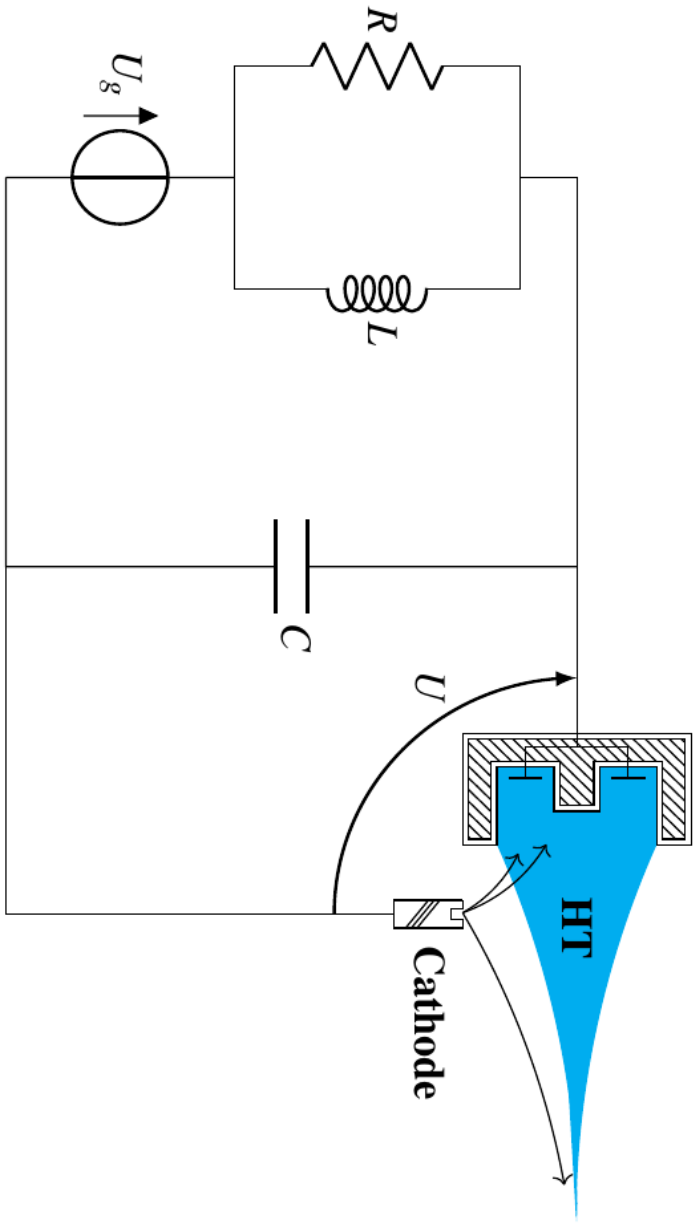

PLEASE CITE THIS ARTICLE AS DOI: 10.1063/5.0119253

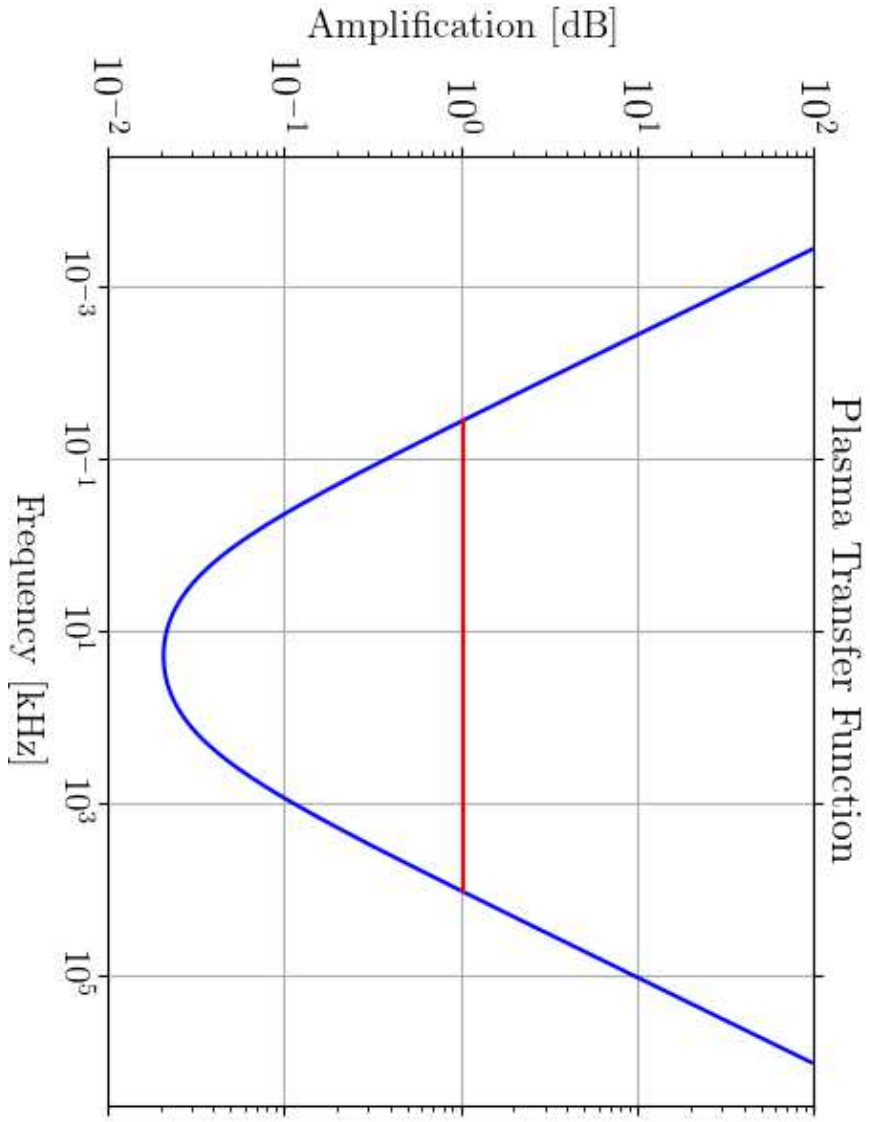

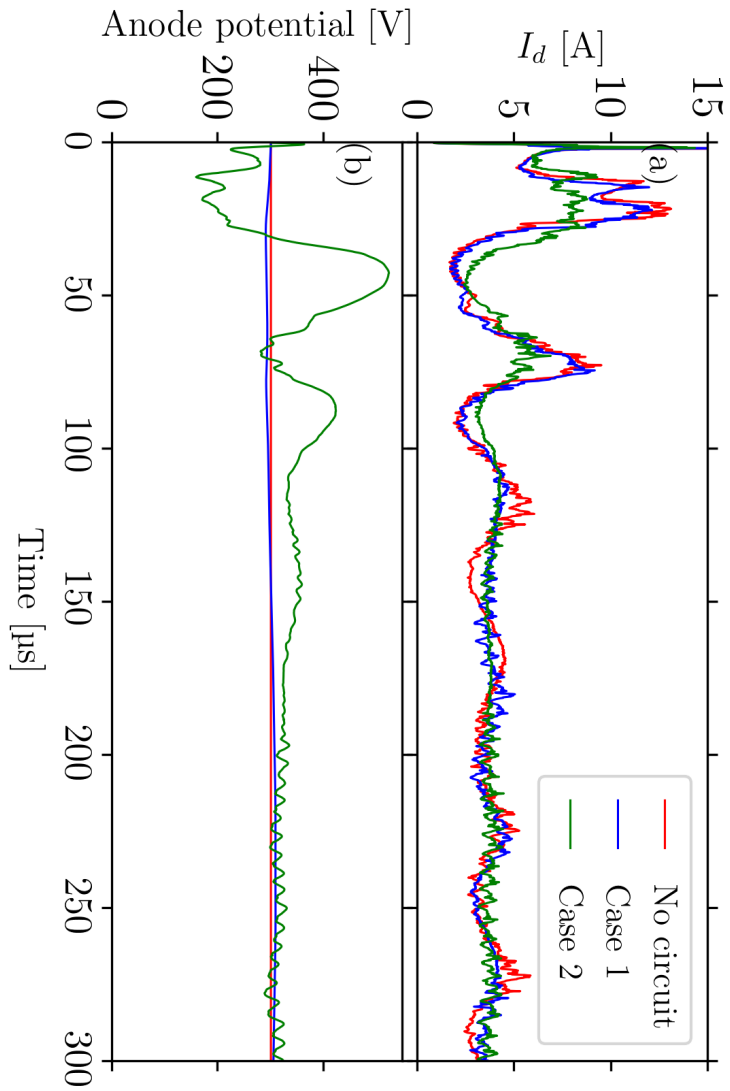

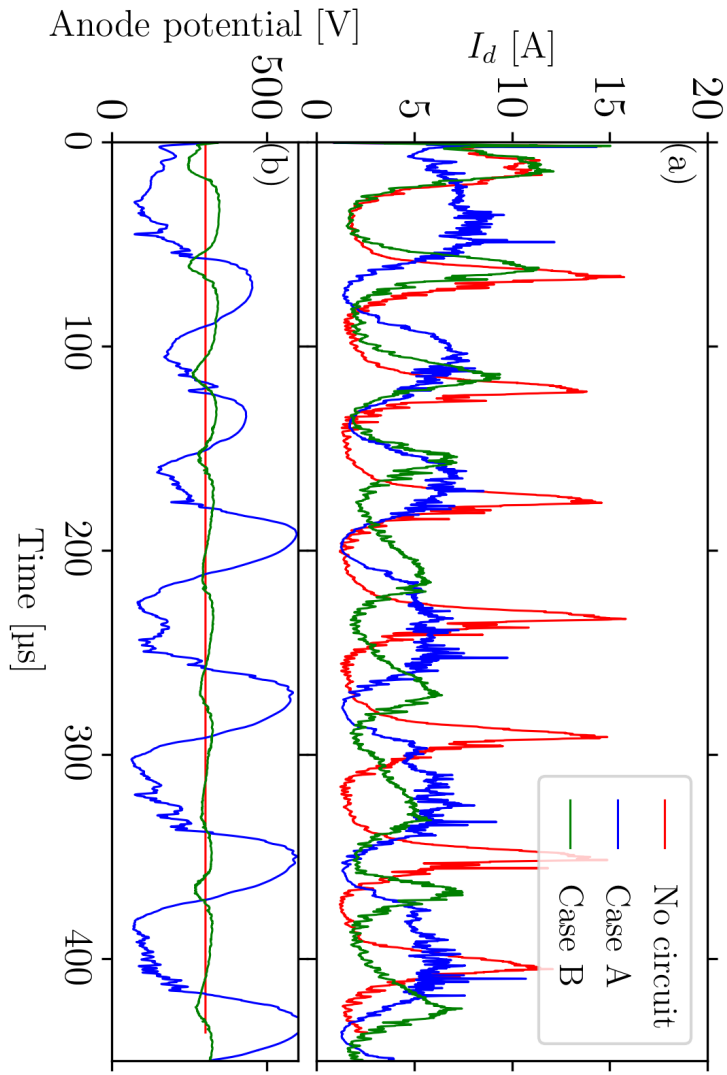

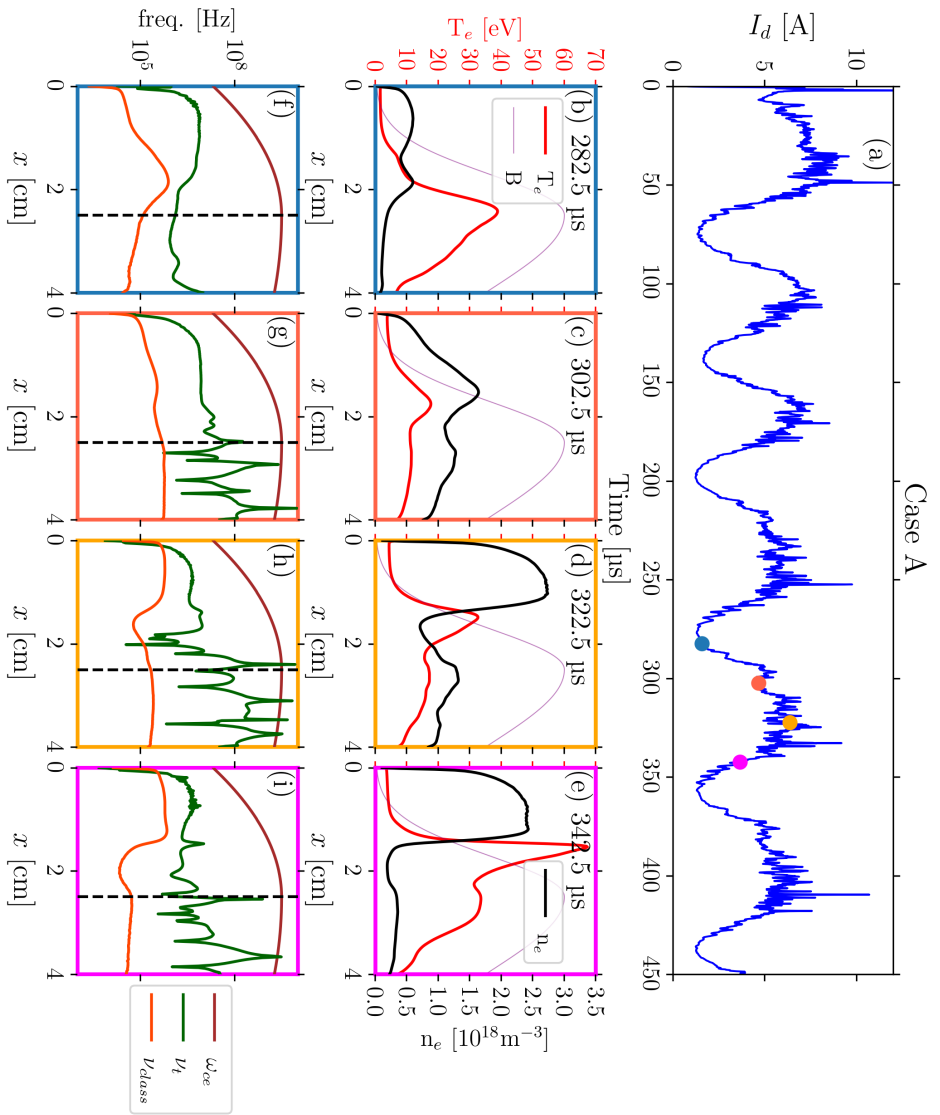

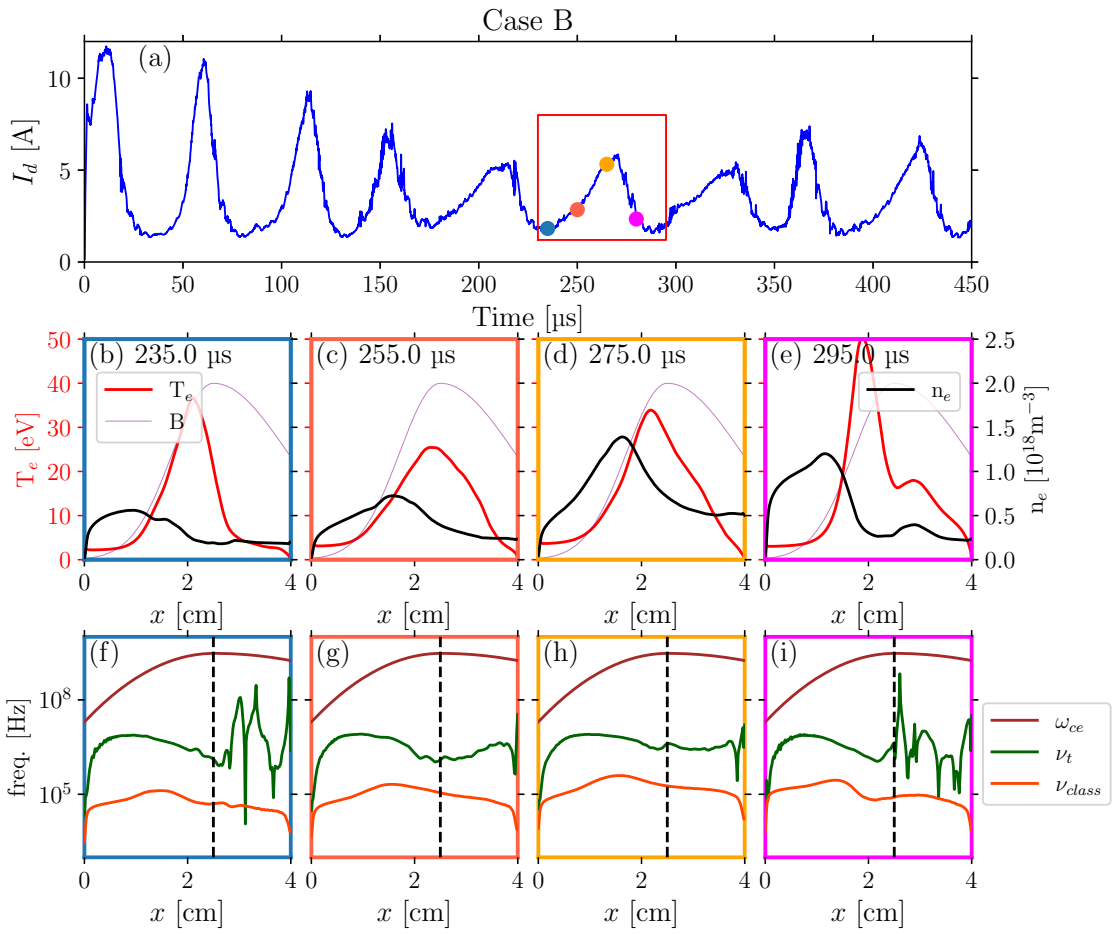

PLEASE CITE THIS ARTICLE AS DOI: 10.1063/5.0119253